AGU100 ADVANCING EARTH AND SPACE SCIENCE

Space Weather

RESEARCH ARTICLE
10.1029/2018SW001937

Special Section:
Space Weather Events of 4-10 September 2017

Ionospheric Response Observed by EISCAT During the 6–8 September 2017 Space Weather Event: Overview

M. Yamauchi[1], T. Sergienko[1], C.-F. Enell[2], A. Schillings[1,3], R. Slapak[2], M. G. Johnsen[4], A. Tjulin[2], and H. Nilsson[1]

[1]Swedish Institute of Space Physics (IRF), Kiruna, Sweden, [2]EISCAT Scientific Association, Kiruna, Sweden, [3]Division of Space Technology, Lulea University of Technology, Kiruna, Sweden, [4]Tromsø Geophysical Observatory (TGO), UiT the Arctic University of Norway, Tromsø, Norway

Abstract We present ionospheric plasma conditions observed by the EISCAT radars in Tromsø and on Svalbard, covering 68°–81° geomagnetic latitude, during 6–8 September 2017. This is a period when X2.2 and X9.3 X-ray flares occurred, two interplanetary coronal mass ejections (ICMEs) arrived at the Earth accompanied by enhancements of MeV-range energetic particle flux in both the solar wind (SEP event) and inner magnetosphere, and an AL $< -2{,}000$ substorm took place. (1) Both X flares caused enhancement of ionospheric electron density for about 10 min. The X9.3 flare also increased temperatures of both electrons and ions over 69°–75° geomagnetic latitude until the X-ray flux decreased below the level of X-class flares. However, the temperature was not enhanced after the previous X2.2 flare in the prenoon sector. (2) At around 75° geomagnetic latitude, the prenoon ion upflow flux slightly increased the day after the X9.3 flare, which is also after the first ICME and a SEP event, while no outstanding enhancement was found at the time of these X flares. (3) The upflow velocity sometimes decreased when the interplanetary magnetic field (IMF) turned southward. (4) Before the first ICME arrival after the SEP event under weak IMF with Bz ~0 nT, a substorm-like expansion of the auroral arc signature took place without local geomagnetic signature near local midnight, while no notable change was observed after the ICME arrival. (5) AL reached $<-2{,}000$ nT only after the arrival of the second ICME with strongly southward IMF. Causality connections between the solar/solar wind event and the ionospheric responses remain unclear.

Key Points:
- The X9.3 flare on 6 September 2017 triggered enhancements of ionospheric electron density and temperature but not ion upflow immediately
- Prenoon ion upflow at 400 km altitude increased over 6–8 September 2017, but its cause can be SEP event rather than CME or X flare
- Substorm-like auroral breakup was observed without notable geomagnetic signature when the interplanetary magnetic field was very weak

Supporting Information:
- Supporting Information S1
- Figure S1
- Data Set S1
- Data Set S2
- Data Set S3

Correspondence to:
M. Yamauchi,
m.yamauchi@irf.se

Citation:
Yamauchi, M., Sergienko, T., Enell, C.-F., Schillings, A., Slapak, R., Johnsen, M. G., et al. (2018). Ionospheric response observed by EISCAT during the 6–8 September 2017 space weather event: Overview. *Space Weather, 16*, 1437–1450. https://doi.org/10.1029/2018SW001937

Received 1 MAY 2018
Accepted 28 AUG 2018
Accepted article online 3 SEP 2018
Published online 27 SEP 2018

1. Introduction

Recent studies show that ionospheric ion escape increases with geomagnetic activity with an exponential dependence on geomagnetic Kp index, with relations of O^+ outflow flux ∝ exp(0.5*Kp) up to Kp ≤ 6 according to the midaltitude Dynamics Explorer 1 satellite with apogee 23,000 km (Yau et al., 1988, see also Moore et al., 1999) and total O^+ loss rate ∝ exp(0.45*Kp) up to Kp ≤ 7 in the manetosheath and high-altitude open magnetosphere such as the exterior cusp and plasma mantle (Slapak et al., 2017). The dependence on Kp is much stronger than that on the interplanetary magnetic field (IMF) north–south (Bz) component (Lennartsson et al., 2004; Slapak et al., 2015; Yau et al., 1988) and even stronger than the high dependence on the solar EUV flux represented by F10.7 index (Cully et al., 2003; Lennartsson et al., 2004; Peterson et al., 2008; Yau et al., 1988).

Such a nonlinear dependence on Kp also exponentially enhances energy extraction from the solar wind to the cusp current system through the mass-loading effect of the escaping ions, i.e., inelastic mixing of escaping ions and incoming solar wind ions (Yamauchi & Slapak, 2018a, 2018b), enhancing the risk of space weather hazards in that local region. Thus, the ionosphere plays two important roles in ion escape, one energizing the ionospheric ions through various energization mechanisms (e.g., André & Yau, 1997) such as Joule heating (Brekke & Rino, 1978) and the other extracting energy from the solar wind through the mass-loading effect of the escaping ions.

Ion escape during space weather events has additional importance because Schillings et al. (2017) found that the escaping O^+ flux for Kp > 7 can be higher than the predicted values from the exponential Kp dependence for Kp ≤ 7. The results suggest that (1) past ion loss from the ionosphere could have been larger than the above estimate (Yamauchi & Slapak, 2018a) and (2) the energy extraction and relevant space weather hazards in the polar region can be even larger than predicted by any existing model using our knowledge for ordinary conditions of Kp < 7. Indeed, there is no guarantee that the response of the high-latitude ionosphere to extreme solar and interplanetary space weather conditions stays within the expected range from ordinary

active conditions through UV ionization, particle precipitations, and electromagnetic energy input represented by, for example, Akasofu's coupling function (Akasofu, 1981; Newell et al., 2007, 2008).

There are many reports on the average ionospheric response to UV flux, particle precipitation, and magnetospheric activity (e.g., Kirkwood & Osepian, 1995; Schunk & Nagy, 2009). Also, many studies exist on the ionospheric responses to space weather conditions that accompanied major magnetic storms for individual parameters that contribute the ion outflow, such as electron density (e.g., Tsurutani et al., 2005), electron and ion temperature (e.g., Wahlund et al., 1992), electric current system and horizontal convection (e.g., Gonzalez et al., 1994), and resultant heatings (e.g., Aikio & Selkälä, 2009; Klumpar et al., 1984).

However, the numbers of event studies of ion outflow during extreme space weather conditions, such as the 6–10 September 2017 event, are far from sufficient. Even for the relatively known ionospheric parameters mentioned above, all the upstream drivers have yet to be identified. Also, the relative importance is not yet clear among possible drivers of the *extraordinary high* ion escape during extreme space weather conditions, for example, enhanced UV, enhanced solar wind (density, bulk velocity, and dynamic pressure) behind interplanetary coronal mass ejections (ICMEs), strong IMF and its southward component Bz, flux enhancement of upstream MeV particles called the solar energetic particle (SEP) events (Futaana et al., 2008; Reames, 1999), flux enhancement of trapped energetic particles in the inner magnetosphere known as the geosynchronous solar proton events (e.g., Turunen, 1993), the main phase of the major magnetic storm with enhanced ring current, a severe substorm, and combinations of these elements.

To make a good assessment of this unsolved question, it is necessary to monitor ion outflow continuously at the most significant locations at different times before and after space weather events when these possible causes occur. In this respect, the 6–8 September 2017 event is ideal for two reasons: (1) because the series of X-class X-ray flares, ICME arrivals, SEP events, and changes of IMF Bz polarity occurred with good separation from each other and (2) because the timing of these events are ideal for both the Cluster satellites and the EISCAT radars (e.g., Wannberg et al., 1997). When the X9.3 flare occurred (details of timing are summarized in section 3), EISCAT observed the local noon sector, where the solar irradiation effect on the ionosphere is maximized. EISCAT observed local midnight when two ICMEs arrived in consecutive days, with the first ICME during northward IMF and the second ICME during strongly southward IMF. On 7 September, many sudden changes of IMF polarities from positive Bz to negative Bz (<-5 nT) took place when EISCAT observed the morning sector, where the upflow flux is statistically highest at this local time at high latitudes. Finally, EISCAT observed the local noon sector when a large southward turning of IMF to purely and stable southward (Bz ~-17 nT) arrived at the Earth on 8 September. For the second ICME, Cluster traversed the cusp and polar cap (the main route of the ion escape) before and after the ICME arrival (Schillings et al., 2018).

Both the EISCAT 224 MHz VHF radar at Tromsø, Norway (69.6°N geographic latitude, or 66.7° corrected geomagnetic latitude: CGLat), and the two 500 MHz antennas on Svalbard (78.2°N geographic latitude, or 75.4° CGLat) were operating during period of the events (e.g., X flares, ICME, and SEP events), running common programme observations in a meridian circle observation configuration. The configuration and observation modes are described in the supporting information (Ogawa et al., 2000; Tjulin, 2017). The VHF radar and the steerable 32 m antenna of the Svalbard radar were pointing at geographic and geomagnetic north, respectively, at a low elevation angle of 30° both of them, thus covering a region of 70°N to 83°N geographic latitude (68° to 82° CGLat) at heights from 70 to about 600 km. The other Svalbard antenna (42 m) is fixed pointing along magnetic zenith. Thus, both latitudinal plasma drifts in the polar cap and local field-aligned phenomena above Svalbard could be observed.

This unique observation in terms of timing and the location of EISCAT gives us the chance to monitor how the ionosphere, particularly the ion flow, responded to the sequence of these events. This paper provides an overview of the EISCAT common programme data with a focus on ion heating and escape, and complementary information to the Cluster observations of the ion escape presented in Schillings et al. (2018).

2. Data

Figure 1 shows the space weather parameters during the 6–8 September 2017, events observed by the GOES-13 geosynchronous satellite Space Environmental Monitor (SEM), Advanced Composition Explorer (ACE) at

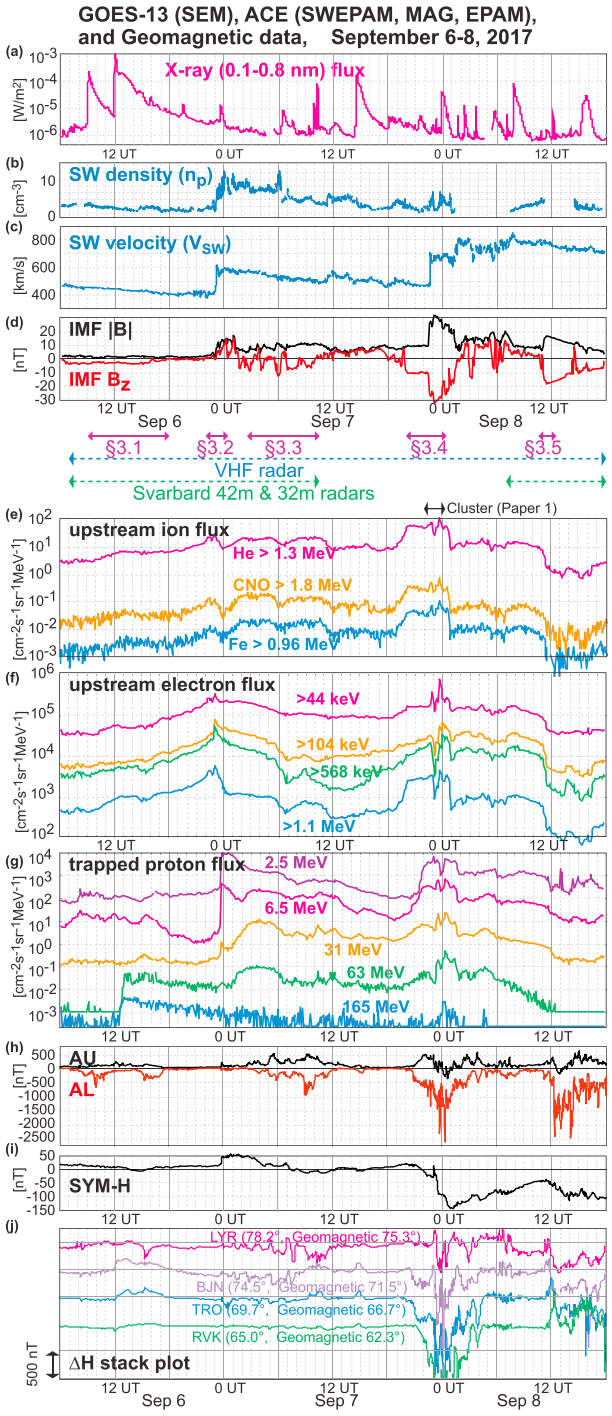

Figure 1. Space weather parameters and geomagnetic data from 6:00 UT, 6 September, to 18:00 UT, 8 September 2017: (a) solar X-ray flux at 1-min resolution, (b) and (c) solar wind proton density and velocity at 1-min resolution, (d) IMF strength and Bz component at 4-min resolution, (e) and (f) upstream energetic ion and electron fluxes at 5-min resolution, respectively, (g) trapped energetic protons in the geostationary orbit at 5-min resolution, (h) provisional AU and AL indices at 1-min resolution, (i) provisional SYM-H index, and (j) 1-min resolution stack plot of geomagnetic horizontal (H) component from four stations in Norway under the same local time as the EISCAT radars' target area (LYR, Longyearbyen; BJN, Bear Island; TRO, Tromsø) and 5° southward (Rorvik geomagnetic station: RVK) as reference. Data are obtained from (a) and (g) GOES-13 geosynchronous satellite SEM, (b)–(f) ACE spacecraft at Sun-Earth first Lagrange point (L1), or (h)–(j) from geomagnetic stations. The travel time from L1 to the Earth is about 30 (800 km/s) to 50 min (470 km/s). The timing for individual events discussed in subsections 3.1–3.5 are marked between panels (d) and (e). The Cluster traversal of the cusp and polar cap (Schillings et al., 2018) is also marked. SEM = Space Environmental Monitor; IMF = interplanetary magnetic field.

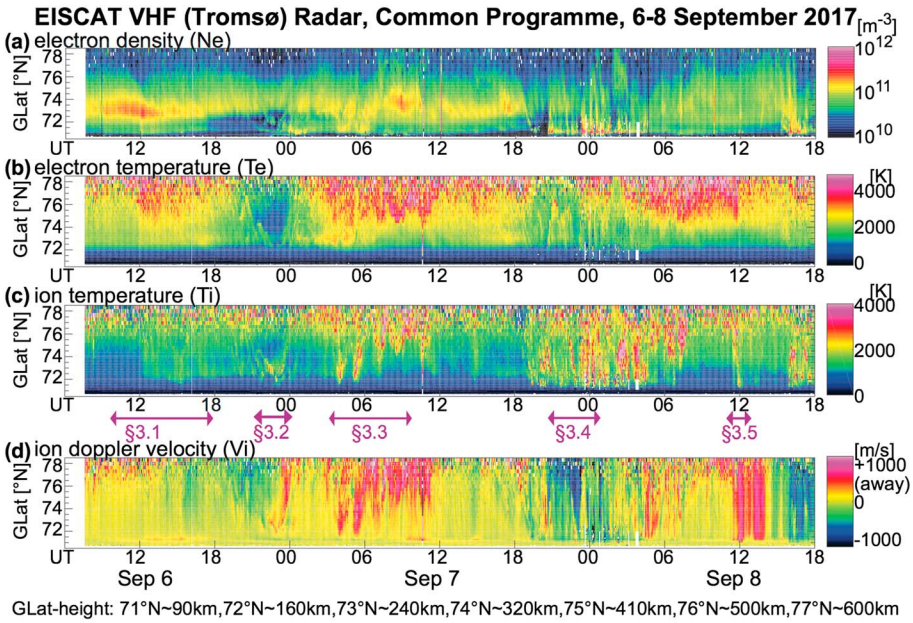

Figure 2. Summary plots of EISCAT Tromsø VHF radar data during 6–8 September 2017. From top to bottom: 5-min averaged values of (a) electron density (N_e), (b) electron temperature (T_e), (c) ion temperature (T_i), and (d) ion Doppler shift velocity in the line-of-sight direction (V_i). The timing for individual events discussed in subsections 3.1–3.5 are marked between panels (c) and (d). Since the VHF radar was looking north with 30° elevation angle, the coverage area is about 69°–70° corrected geomagnetic latitude (CGLat) for 80–200 km altitude and 70°–72° CGLat for 200–400 km altitude. The upflow and poleward flow cannot be distinguished from this data because both give *away-flow*. GLat = geographic latitude.

the Sun-Earth first Lagrange point (L1), and geomagnetic indices. The GOES-13 SEM data are shown in Figures 1a and 1g for solar X-ray flux and for trapped MeV proton flux in the geostationary orbit, respectively. ACE data are shown in Figures 1b–1f for (b) solar wind proton density, (c) solar wind velocity, (d) IMF strength and Bz component, (e) upstream MeV ions fluxes, and (f) upstream high energy electron fluxes, respectively. Geomagnetic indices are shown in Figure 1h for AU and AL indices and in Figure 1i for SYM-H index which is a 1-min resolution substitute for Dst index. In addition, Figure 1j shows a stack plot of 1-min resolution geomagnetic horizontal (H) component data from four Norwegian stations under the same local time zone as the target area of the EISCAT radars. The time resolution is 1 min for Figures 1a–1c and 1h–1j, 4 min for Figure 1d, and 5 min for Figures 1e–1g, respectively. In Figures 1e–1g, where energetic particle fluxes are presented, only selected energy ranges from the entire observation are presented. Explanation of the geomagnetic indices is found in Davis and Sugiura (1966) for AU and AL that represent the substorm activity and in Iyemori (1990) for SYM-H that represents the ring current activity.

In Figure 1, double-headed arrows below panel (d), with the markings §3.1, §3.2, §3.3, §3.4, and §3.5, denote the period relevant to individual space weather events that are studied in this paper in subsections 3.1–3.5, respectively. Figure 1 also indicates, above panel (e), the operation periods of the EISCAT common programme and Cluster traversals over the northern polar cap and the cusp. All five events are covered by three EISCAT antennas except for the fourth event, which is covered only by the VHF radar (Tromsø) and Cluster.

Figures 2–4 show 5-min averaged summary plots of EISCAT data during 6–8 September 2017 from the Tromsø VHF radar, the Svalbard 42 m antenna, and the Svalbard 32 m antenna, respectively. In each figure, from top to bottom, the following analyzed parameters are shown: (a) electron density (N_e in m^{-3}), (b) electron temperature (T_e in K), (c) ion temperature (T_i in K), and (d) ion Doppler shift velocity in the line-of-sight direction (V_i in m/s with positive direction away from the radar). The local time in hours (LT) and UT are different by about 1 hr (LT ≈ UT + 1), and hence 11:00 UT corresponds approximately to the local noon. The explanation of the EISCAT configuration and operation mode is given in the supporting information.

With respect to the viewing angle, vertical axes are displayed as geographic latitude for the VHF radar and Svalbard 32 m antenna, and as altitude for the Svalbard 42 m antenna. Since the signal becomes noisy

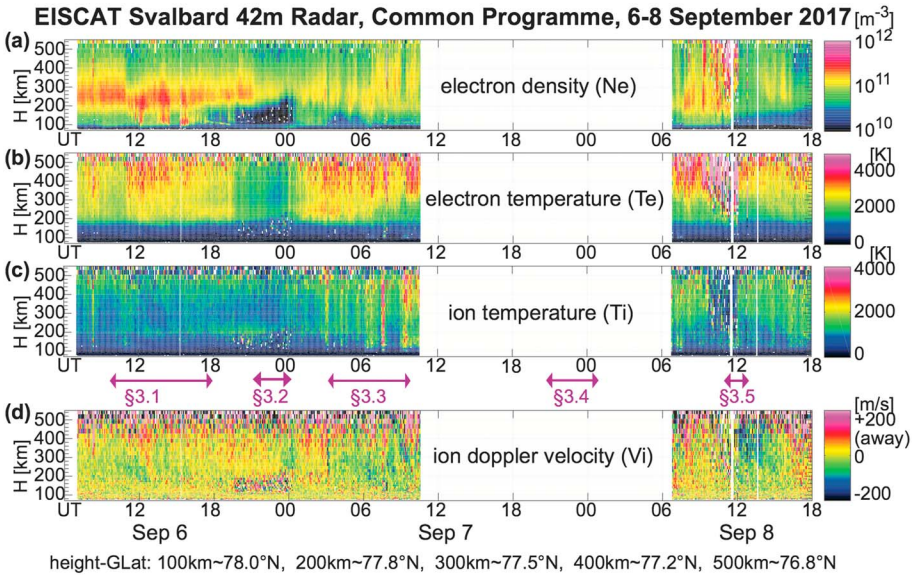

Figure 3. The same as Figure 1 for the 42 m antenna of the 500 MHz Svalbard radar, pointing upward along the geomagnetic field. Unlike the Tromsø radar, the Svalbard radar was not operating all the time, as indicated by the data gap. GLat = geographic latitude.

above 500 km, we limit our discussion to below 400 km altitude, which corresponds to approximately 71–75°N geographic latitude (approximately 68°–72° CGLat) for the VHF radar in Figure 2, 77–78°N geographic latitude (~75° CGLat) for the Svalbard 42 m antenna in Figure 3, and 79–83°N geographic latitude (77°–81° CGLat) for the Svalbard 32 m antenna in Figure 4.

Since horizontal flow velocity (in the order of 100 m/s) is normally faster than vertical velocity (in the order of 10 m/s as confirmed by the Svalbard 42 m antenna that is looking in the vertical direction), the 30° elevation angle of the VHF radar (Figure 2) and Svalbard 32 m antenna (Figure 4) means that the Doppler shift velocity

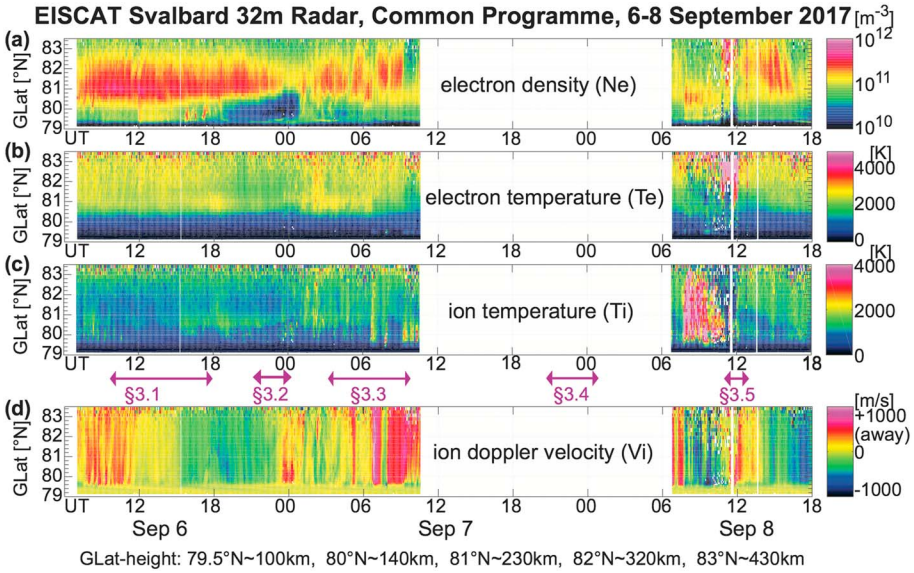

Figure 4. The same as Figure 1 for the 32 m antenna of the 500 MHz Svalbard radar, pointing at geomagnetic north with 30° elevation angle. The coverage area is about 77°–79° corrected geomagnetic latitude (CGLat) for 80–200 km altitude and 79°–81° CGLat for 200–400 km altitude. Unlike the Tromsø radar, the Svalbard radar was not operating all the time, as indicated by the data gap. GLat = geographic latitude.

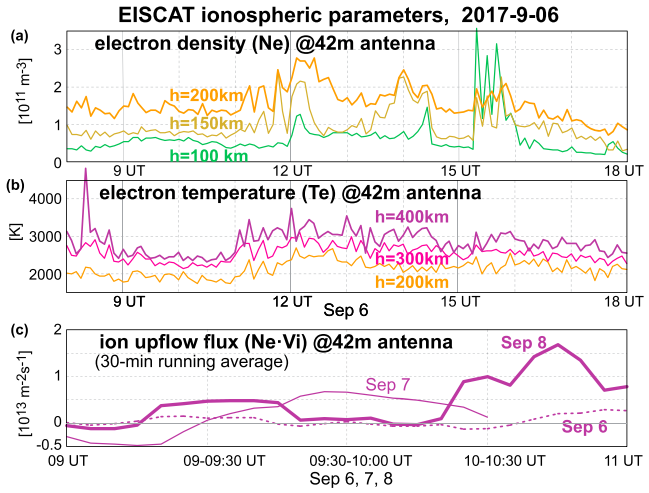

Figure 5. Line plots of (a) electron density (N_e) and (b) electron temperature (T_e) for selected altitudes from the Svalbard 42 m antenna data during 08:00–18:00 UT, 6 September 2017. (d) Running average of the estimated upflow flux (=$N_e \cdot V_i$) at 400 km altitude from the Svalbard 42 m antenna data during 08:30–11:00 UT for three consecutive days (6–8 September 2017).

largely reflects horizontal (northward) flow velocity. In the present case, we discuss convection signatures of >200 m/s only, and hence we can safely interpret Figures 2d and 4d as northward flow velocities.

To make some of the features in Figures 2–4 more visible in quantitative manner, Figures 5 and 6 show line plots of some of the EISCAT observations at selected altitude and time for §3.1 (Figure 5) and §3.3 (Figure 6).

3. Observations

We identified five independent events during the period of 6–8 September 2017 as marked in Figure 1: X2.2 and X9.3 X-ray flares occurred around 09 and 12 UT with peak at 09:10 and 12:01 UT at the Earth, respectively (§3.1); Two ICMEs arrived long after these flares at around 23:50 UT on 6 September and 23:10 UT on 7 September with 5 min accuracy, with the first ICME during northward IMF (§3.2) and the second ICME during strongly southward IMF (§3.4); Many sudden changes of the IMF polarity from northward to southward (Bz < -5 nT) occurred on 7 September (§3.3 and one large change from slightly northward IMF to purely and stable southward IMF (Bz ~-17 nT) at around 11:40 UT at the Earth (§3.5). Among these, some events include subevents, such as large changes in different parameters. The timing of these events and subevents is summarized in Table 1.

Immediately after the second ICME with enhanced southward IMF arriving at the Earth at around 23:10 UT on 7 September (Figures 1c and 1d), magnetic storm main phase started at 23:19 UT (reaching SYM-H < -90 nT at 23:32 UT, Figure 1i) and a severe substorm started at 23:38 UT (reaching AL $< -2{,}000$ nT at 23:43 UT, Figure 1h). Thus, separation of the effects between individual ICMEs and the storm/substorm is not simple.

Important subevents relevant to the ionospheric heating and ion escape are SEP events, that is, limited to in this paper, flux enhancements of MeV-range energetic particles in the solar wind, because Venus and Mars studies have shown enhanced ion escape by the SEP event rather than ICME for the December 2006 space weather event (Futaana et al., 2008). Since energetic particles in the solar wind can access the cusp and polar cap where the ion escape is the most intense, we expect the same effect for the Earth. SEP events are related to §3.2, §3.4, and §3.5 in Figure 1.

The event marked as §3.2 around the first ICME arrival on 6 September (23:09 UT at ACE spacecraft, Figure 1c) includes gradual increases of energetic particle flux in the solar wind from around 20 UT with the first peak at 22:20 UT (Figures 1e and 1f) and a geosynchronous solar proton event at 23:35 UT (Figure 1g). Since the timing of the flux increase of the energetic particle is quite different between ACE and GOES, we use different terminologies: *SEP event* in the solar wind (ACE observation) and *proton event* at the geosynchronous orbit (GOES observation).

The peak of the SEP event is observed nearly simultaneously with the first ICME by the ACE spacecraft. Therefore, these MeV particles (with much shorter travel time than the ICME) must have been locally accelerated by the ICME shock rather than by the solar flare at the solar surface (Reames, 1999). With this similar timing between the ICME and the SEP event, it is difficult to identify the direct cause of the ionospheric responses. Still, the magnetic storm sudden commencement at 23:45 UT (Figure 1i) is most likely the result of the first ICME arrival at the Earth (estimated at around 23:50 UT on 6 September).

The same coincidence with the SEP event (first peak 22:45 UT on 7 September at ACE) or geosynchronous proton event (start at 23:20 UT at GOES-13) is also found for the event marked by §3.4 around the second ICME arrival (22:36 UT at ACE and about 23:10 at the Earth), which is also accompanied by a significant enhancement of southward IMF, as shown in Figure 1d. Unlike the first ICME arrival, the flux of the MeV particles (Figure 1g) was already high from around 20 UT on 7 September at the ACE spacecraft and around 21:30 UT at geosynchronous orbit. The ACE spacecraft also detected a large southward turning of IMF simultaneous with this SEP event at 19:56 UT on 7 September (a short period of southward IMF during 19:20–19:34 UT), indicating that it originated from the solar surface (the magnetic connectivity to the source

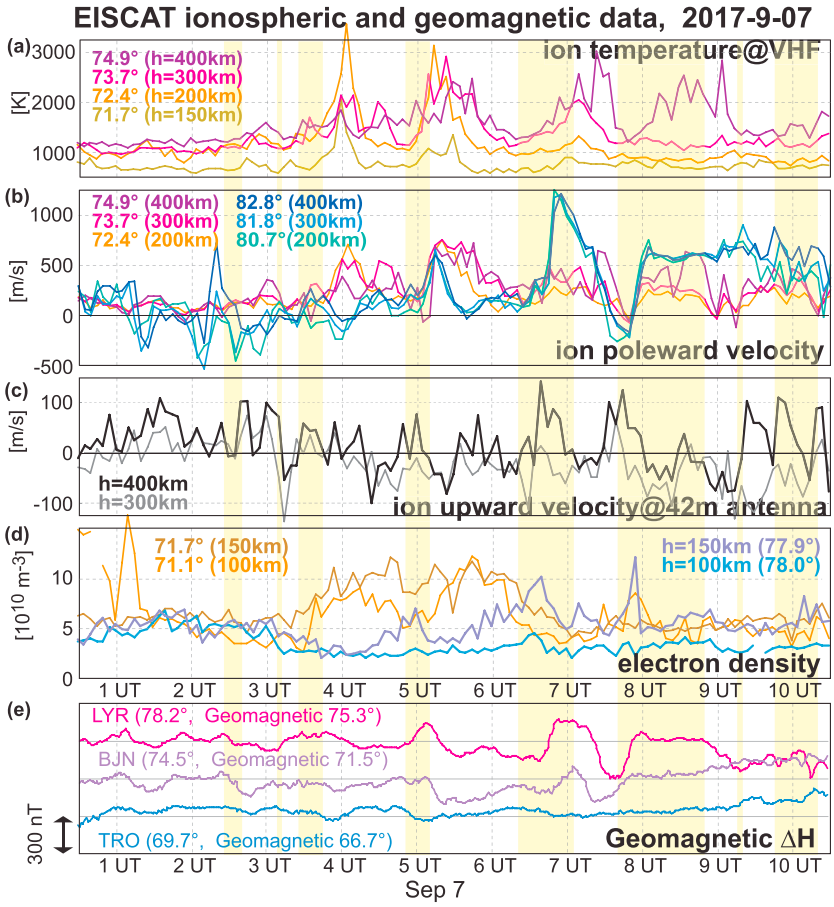

Figure 6. Line plots of (a) T_i data from the Tromsø VHF radar in Figure 2, (b) V_i data from the Tromsø VHF radar and the Svalbard 32 m antenna in Figures 2 and 4, (c) V_i data from the Svalbard 42 m antenna in Figure 3, and (d) N_e data from the Tromsø VHF radar and the Svalbard 42 m antenna in Figures 2 and 3, for selected altitudes and limited time periods. (e) Expanded plot of Figure 1j of geomagnetic horizontal (H) deviation. EISCAT; LYR = Longyearbyen geomagnetic station; BJN = Bear Island geomagnetic station; TRO = Tromsø geomagnetic station.

region of the energetic particles determines their path to the Earth) rather than accelerated locally. If the source region is connected by the IMF only to L1 but not the Earth, the geosynchronous proton event may start much later than the arrival of the IMF change at the Earth. This means that the event marked by §3.4 can be subdivided into (a) increase of MeV particles near the Earth at around 21:30 UT and (b) second ICME with enhanced southward IMF arriving at the Earth at around 23:10 UT.

Finally, a sudden southward turning of IMF at 11:08 UT on 8 September (to Bz < -8 nT at ACE spacecraft, Figure 1d) marked as §3.5 is also accompanied by a sharp decrease of energetic particle flux in the solar wind at 11:10 UT, marking the end of the SEP event, and moderate decrease of the geosynchronous proton event at around 11:50 UT, that is, the estimated arrival time. This is again most likely related to the magnetic connection to the solar surface. Identifying the direct cause of the ionospheric effect is not straightforward.

3.1. Solar Flares on 6 September (around 09 and 12 UT)

When the X9.3 flare took place at around 12 UT, EISCAT was observing the local noon sector at around 13 LT. Therefore, direct ionospheric effects of the enhanced radiation flux are expected, such as an increase in the total electron content (Tsurutani et al., 2005). In fact, the EISCAT radars detected at around 12 UT a short-lived enhancement of electron density in a wide latitude range (71–73, 78, 79–81°N) below 200 km altitude in Figures 2a, 3a, and 4a. To make this more visible, Figure 5a shows the line plots of electron density for a 10-hr period on 6 September at 100, 150, and 200 km altitudes, respectively, observed by the Svalbard 42 m antenna (cf. Figure 3). The duration of this short-lived enhancement is the same as that of the flare

Table 1
Approximate Arrival Time of Each Solar Wind Event to the Earth (UT)

Event	Day 2017	Arrival UT	Event	IMF Bz
§3.1	6 Sep.	~09:00	**X2.2 flare**	<0 nT
§3.1	6 Sep.	~11:55	**X9.3 flare**	<0 nT
§3.1	6 Sep.	~18:00	**X-ray < M-class**	~0 nT (B ~3 nT)
§3.2	6 Sep.	~20:00[a]	SEP enhancement	~0 nT (B ~3 nT)
§3.2	6 Sep.	~22:20[a]	SEP peak	~0 nT (B ~3 nT)
§3.2	6 Sep.	~23:35	Proton event	~0 nT (B ~5 nT)
§3.2	6 Sep.	~23:50	**First ICME**	>5 nT (from near zero)
§3.3	7 Sep.	~02:25	Bz change	<−5 nT
§3.3	7 Sep.	~03:00	Bz change	~−3 nT
§3.3	7 Sep.	~03:25	Bz enhance	<−5 nT
§3.3	7 Sep.	~04:50	Bz change	<−5 nT
§3.3	7 Sep.	~06:20	Bz change	<−5 nT
§3.3	7 Sep.	~07:40	Bz change	<−5 nT
§3.3	7 Sep.	~09:15	Short Bz spike	~−3 nT
§3.3	7 Sep.	~09:45	Bz change	<−5 nT
§3.3	7 Sep.	~10:45	Bz change	Positive
	7 Sep.	~14:30	**(X1.3 flare)**	Positive
§3.4	7 Sep.	~20:45	Bz change	<−8 nT
§3.4	7 Sep.	21:00–22:00[a]	SEP peak	−9 nT
§3.4	7 Sep.	~21:30	SEP arrival	−9 nT
§3.4	7 Sep.	~23:10	**Second ICME**	<−25 nT (from −9 nT)
§3.5	8 Sep.	~11:10[a]	End of SEP event	Positive
§3.5	8 Sep.	~11:20	Bz change	<−5 nT (later −17 nT)

Note. IMF = interplanetary magnetic field; SEP = MeV-range energetic particle in the solar wind; ICME = interplanetary coronal mass ejection. Bold face = major space weather events.
[a]At ACE spacecraft (first Lagrange point L1).

burst (in the order of 10 min). A similar but faint enhancement in electron density was also detected at around 09:10 UT in the Tromsø radar (Figure 2) when another X flare (X2.2 flare) occurred.

Simultaneously, electron temperature (T_e) enhancement was also detected by the Tromsø radar (Figure 2) and to a lesser degree by the Svalbard 32 m antenna (Figure 4) at around 12 UT, lasting until around 18 UT. Although 18 UT is close to local sunset on the ground, sunset at 100 km over Tromsø is as late as around 21 UT and there is no sunset 100 km above the Svalbard radars. Rather, these enhancements might be related to the solar irradiation because Figure 1a shows that the X-ray flux exceeded M-class flare level until around 17 UT. The Svalbard 42 m antenna looking at 75° CGLat (Figures 3 and 5b) detected a similar enhancement of T_e (and a less outstanding enhancement of ion temperature T_i). Although the signature started already at around 11 UT before the X9.3 flare, the signature until around 12 UT is most likely related to the cusp with enhanced electron density and with strong altitude dependence (Nilsson et al., 1996). This interpretation agrees with the higher T_e at higher latitude in the subcusp region during approximately 11–12 UT in Figure 2, while there is no signature in the polar cap in Figure 4 at the same time. The latter suggests that Figure 4 shows polar cap rather than the cusp during that period.

However, none of the EISCAT radars detected notable T_e enhancement at around 09 UT when the X2.2 flare occurred. If the solar irradiation is driving the T_e enhancement, the same level of irradiance (e.g., approximately 12–15 and 09–10 UT in Figure 1a) should cause a similar level of T_e enhancement, which is not the case for the present observation. Even taking into account the solar zenith angle, the irradiation flux alone does not explain the absence of a temperature enhancement after 09:00 UT. This problem must be investigated in the future.

Another low-altitude ionospheric effect caused by the X flares is enhancement of ion convection V_i at a limited altitude range (90–130 km) in the ionospheric E-region in both Figures 2d and 4d (the target latitudes are about 68° and 77° CGLat, respectively) without variation of the peak altitude of V_i. The constant altitude of the convection enhancement seen in two radars without heating signatures at the same location indicates that this enhanced convection flows in a horizontal (northward) direction at a limited altitude range. In fact, the Svalbard 42 m antenna (Figure 3d) did not detect any signature of upward flow at this altitude. The enhanced convection signature became outstanding after 12:00 UT, but already existed from around 09 UT when the X2.2 flare occurred.

One possible cause of this velocity enhancement limited to the E-region is the enhancement of the Sq convection and resultant Sq current through extra heating of the atmosphere and conductivity enhancement (Dmitriev & Yeh, 2008; Enell et al., 2008). In fact, the geomagnetic data in Figure 1j show an outstanding enhancement of the Sq variation at around 12 UT on 6 September, corresponding to the timing of the X9.3 flare. This Sq enhancement is strongest at Bear Island geomagnetic station (BJN) at 74.5°N latitude (or 71.5° CGLat) and is notable over 63–76°N (or 60–73° CGLat). There are several explanations for this latitudinal limitation such as the geometry of the convection cell having a sink near the terminator and the latitude-limited flux enhancement of energetic particles.

Although we see enhancements of electron density N_e and temperature T_e subsequent to the X9.3 flare after 12:00 UT on 6 September, no notable change was detected in the upflow velocity from the Svalbard 42 m antenna in Figure 3d. Still, if we compare the upflow flux between different days, those in the prenoon region show higher values on 7 September (maximum $7{\cdot}10^{12}{\cdot}m^{-2}{\cdot}s^{-1}$ in a 30-min average) and 8 September (maximum $1.7{\cdot}10^{13}{\cdot}m^{-2}{\cdot}s^{-1}$ in a 30-min average, and later reached $4{\cdot}10^{13}{\cdot}m^{-2}{\cdot}s^{-1}$) than 6 September (maximum $3{\cdot}10^{12}{\cdot}m^{-2}{\cdot}s^{-1}$ in a 30-min average), as shown in Figure 5c. For this examination, we took a 30-min running average of $N_e{\cdot}V_i$ at 400 km altitude from the Svalbard 42 m antenna between 08:30 and

11:00 UT (about 10–12 LT), because the outflow is maximized at this local time for this latitude according to the past statistics (e.g., Moore et al., 1999, and references therein). The simultaneous Cluster observation of the same event at high altitudes in the prenoon region shows that the ICME arrivals caused an increase of ionospheric ion outflow (Schillings et al., 2018). Therefore, the increased solar irradiation most likely contributed to preconditions for enhancement of the ion outflow. In fact, we detected an increase of ion temperature (T_i) after the X9.3 flare on 6 September in the VHF radar (Figure 2), which covered the subcusp region at around 12 UT. In this sense, the observation is consistent with solar irradiation (F10.7 index) control of the upflow (Cully et al., 2003; Peterson et al., 2006, 2008).

3.2. Arrival of the First ICME on 6 September (After 23:00 UT)

According to systematic observations and modeling of the solar surface and interplanetary propagation (Redmon et al., 2018; Schillings et al., 2018), the first ICME was most likely ejected from the Sun in the evening of 4 September (cf. M5.5 flare at around 20:30 UT), while the second ICME was most likely ejected at midday on 6 September (cf. the X9.3 flare). For both ICMEs, local time of the EISCAT radars was near local midnight when the ICME arrived at the Earth.

Before the first ICME arrived at ~23:45 UT on 6 September, strong toward (southward) convection of 200–600 m/s (these high values suggest horizontal flow) was observed at 77°–81° CGLat (Figure 4) from around 15 UT to around 23 UT, that means, antisunward convection in the nightside sector. At equatorward of this antisunward convection, a strong sunward flow (red in the color scale in Figure 2) was detected at a limited line-of-sight distance (i.e., limited latitude), first approaching the Tromsø radar from about 21:30 UT, and later departing from the radar from about 23:10 UT. N_e, T_e, and T_i followed the same time-distance profile, moving equatorward slowly before the ICME arrival, followed by quick poleward expansion with enhanced intensity, that is, in the same manner as the latitudinal motion of an auroral arc near midnight. The lowest latitude (auroral breakup latitude) is about 70° CGLat, which is much higher than the ordinary onset of about 65° CGLat (Akasofu, 1981) but could be reasonable if we consider the weak IMF (about 3 nT) with Bz nearly zero. In the polar cap (Figure 4), a significant enhancement of the sunward convection was also detected at a wide latitudinal range. However, no geomagnetic signature was detected at around 23 UT on 6 September in the nearby stations (Figure 1j) before the sudden commencement signature at about 23:45 UT, that is, after the start of auroral expansion. Without a corresponding geomagnetic signature, this is only a *substorm-like* expansion but is not necessary an auroral substorm (Akasofu, 1981).

The onset of this expansion together with the observed change in the convection direction took place before the arrival of the first ICME or the flux enhancement of geosynchronous energetic particles. The IMF during the entire period was very weak as mentioned above. Therefore, this is not triggered by the solar wind or the IMF condition. The only possible external driver we found so far is the SEP event, with increase of flux gradually from around 20 UT with peaks at around 22:20 and 23 UT at ACE (L1) in Figures 1e and 1f.

As for the ion upflow, the Svalbard 42 m antenna (Figure 3) observed a very weak away flow (~20 m/s on average) at around 200–400 km from about 19 UT until this onset, but became a weak toward flow during the expansion of the auroral arc (about 23:20–00:40 UT on 6–7 September). This could well be an artifact of the horizontal flow that is one order of magnitude faster than the upflow. In any case, we could not detect any enhancement of upflow of more than 20 m/s at the arrival of the first ICME, but this is not surprising because it is near the midnight sector where the auroral-related ion escape takes place in much lower latitudes than the Svalbard radar (e.g., Moore et al., 1999).

3.3. Repeated Convection Enhancement With 1.5-hr Period

In the morning to noon sector between around 03 and 11 UT, on 7 September, the Tromsø VHF radar (Figure 2) detected intermittent enhancements of T_i and away-flow with lifetimes of about 1 hr each, starting at around 03:30, 05, 06:30, 08, 09:10, and 10:20 UT, as shown in Figures 6a (for T_i) and 6b (for V_i). The ion velocity exceeds 500 m/s, and hence we can assume the flow bursts are poleward. This explains why Figure 2a (N_e) does not show the same structure (N_e mainly reflects the altitude profile). In addition, latitude-time dispersion of the enhancement is seen for each flow burst, indicating that the flow is patchy, and limited in longitude.

The ground magnetometers at Longyearbyen under the Svalbard radars and BJN also detected variations synchronized with the horizontal (poleward) convection, but this variation was not detected at Tromsø at

69.7°N latitude (or 66.7° CGLat), as is shown in Figure 6e. Since the VHF radar detected the flow from 71°N, the equatorward edge of the flow is located at 70–71°N for the first burst (peak at around 04 UT on 7 September). As the radar approaches noon, the start latitude of these patches of poleward flow burst increases, indicating a gradual poleward shift of the equator edge of the convection reversal.

Similar intermittent convection enhancements were observed by the Svalbard 32 m antenna (Figures 4d and 6b), but simultaneously at all latitudes, indicating a simultaneous motion of the entire region. The start time of these flow bursts is the same as, but the end time much earlier than, those observed at lower latitude (Figure 2d). The start time of these flow bursts agrees well with the southward turning of IMF (marked by hatches in yellow in Figure 6 and listed in Table 1).

Figures 3d, 6c, and 6d show many short-lived enhancements of upflow (up to 100 m/s at 400 km altitude) together with N_e enhancement in the Svalbard 42 m antenna that is looking in the vertical direction. The timings of the V_i enhancement do not match those of the intermittent flow bursts. Rather, the upflow velocity started increasing before the southward turning of IMF (hatched in yellow in Figure 6) and reversed to decreasing when the IMF turned to southward. Since the phase of V_i enhancement does not match between the Svalbard 42 and 32 m antennas, this unexpected behaviors of ion drift measured by the Svalbard 42 m antenna is not due to contamination by the strong poleward flow, although we have not identified any other explanation. This must be studied in detail but is outside the scope of this overview paper.

The flow velocity variation has changed slightly during the strong substorm during around 09–10 UT (AL ~ −1,000 nT at 08:55 UT). The poleward flow velocity was constantly high in the polar cap at >80°N (Svalbard 32 m antenna), whereas the intermittent velocity enhancement pattern repeated at lower latitudes, which most likely correspond to the boundary region of the polar cap (both VHF and Svalbard 42 m antennas). The peak velocity during this substorm is at the same level as before the substorm onset in both horizontal and upward directions.

3.4. Arrival of the Second ICME on 7 September (~23 UT)

This ICME with higher velocity than the previous day is again accompanied by a SEP event (Figures 1e and 1f) and a geosynchronous proton event (Figure 1g). Meanwhile, the IMF conditions differed considerably from the previous one, with a large southward IMF of about Bz ~−30 nT, triggering the major geomagnetic storm (start of main phase at 23:19 UT according to SYM-H in Figure 1i) as well as the AL < −2,000 nT substorm (starting at 23:38 UT with its peak at 23:43 UT in Figure 1h) on 7 September.

For this event, only Tromsø VHF radar data (Figure 2) are available. The Svalbard radar resumed about 7 hr after the ICME arrival. Nevertheless, the similar local time of the EISCAT measurements to the previous ICME arrival the day before allows us to make a unique comparison. Figure 2d shows that strong antisunward (equatorward) convection preexisted from 21:40 UT on 7 September at higher latitude than 76°N (73° CGLat), with higher velocity than the previous event on 6 September, which is typical for a prolonged southward IMF. The timing is consistent with a southward switch of the IMF at ACE at 19:56 UT.

On the arrival of the second ICME (or SEP event or geosynchronous proton event), N_e, T_e, and T_i are enhanced, for about half an hour from 23:20 UT on 7 September. These enhancements are seen at a relatively wide range of line-of-sight distances, implying that the aurora is probably distributed over a relatively wide latitudinal range, which agrees with the signature of disturbed convection in V_i. Thus, this is just another typical case of strong substorm activity.

3.5. Sudden Equatorward Shift of the Cusp on 8 September (~12 UT)

Finally, the strongest ion away-flow (antisunward convection) since the X9.3 flare was observed near local noon by the Tromsø radar (Figure 2d), starting around 11:30 UT on 8 September. Similar enhancement of the antisunward convection was also observed by the Svalbard 32 m antenna (Figure 4d), and thus observed at a wide latitude range over 71–82°N (69°–80° CGLat). The geomagnetic data (Figures 1h and 1j) show the onset of a strong substorm at 12:13 UT that led to the second main phase of the magnetic storm seen in SYM-H, but this onset is only after the enhancement of the ion away-flow. The timing of the enhanced poleward flow matches with the significant change in the IMF as summarized in Table 1: it became southward, first to Bz ~−5 nT at 11:20 UT and later to Bz ~−15 nT at 11:40 UT.

However, the enhancement is only for antisunward flow. Both Svalbard antennas (42 and 32 m) show that the cusp signature (N_e and T_i) moved equatorward and faded at around the same time (11–12 UT). Ion upflow (Figure 3d) also decreased. The observation follows the statistical cusp view, which is expected to move equatorward outside the target area of the Svalbard 42 m antenna in such conditions (Newell et al., 1989). The upflow velocity after the cusp moved equatorward is also lower than before entering the cusp, which corresponds to the prenoon side of the cusp when the IMF was pointing northward.

4. Discussion

The September 2017 space weather event turned out to be an ideal event to study the ionospheric ion responses to extreme space weather conditions using the EISCAT radars because an X9.3 flare, two ICME arrivals, and peaks of the SEP events all took place when the EISCAT radars were observing near local noon or near local midnight. For example, sudden increases of the X-ray flux by two orders of the magnitude and associated increases of the UV flux did not change the upflow signature at $<$400 km altitude, although the ion and electron temperatures were enhanced immediately after the X9.3 flare, providing a favorable precondition for ion escape. The absence of a significant increase of ion upflow agrees with the Cluster result (Schillings et al., 2018). The observations suggest that the high X-ray (and UV) flux can simply be a precondition before enhancing the ion upflow.

An intense upflow was observed between around 05 and 12 UT on 7 September, when the geomagnetic activity was relatively low whereas substorms starting at around 09 UT on 7 September (AL ~ $-$1,000 nT at 08:55 UT) and around 12 UT on 8 September (AL ~ $-$2,400 nT at 12:17 UT) did not cause notable enhancement of ion outflow although the development of AL was sharp and EISCAT was observing the midday sector. This indicates that the reported Kp dependence comes from common upstream space weather conditions that cause both high escape rate and the geomagnetic activity.

No immediate enhancement of ion upflow in the local midnight sector is detected after the arrival of the first ICME or SEP event (Figures 1e–1g). Meanwhile, the upflow in the prenoon sector (corresponding to approximately 7–10 UT) became somewhat higher on 7 September than on 6 September before the first ICME (and the X9.3 flare). Thus, the effect of the enhancement, if the ICME arrival or SEP event contributed to the upflow, continued for hours. In fact, Cluster observed higher escape flux after the second ICME arrival than before.

The observations could not identify the dominating element that contributed to the upflow enhancement from among the solar wind velocity increase, density increase, or the SEP events that peaked at the passage of the first ICME. There are reports that SEP events originating from the solar surface enhance ion escape from planets (Futaana et al., 2008; Ulusen et al., 2012). Since energetic particles can penetrate into the lower part of the ionosphere/atmosphere and have larger gyroradius to reach the subcusp region compared to the solar wind, it is quite possible that energetic particles that are accelerated at the ICME shock also contributes to the upflow. If so, the relatively smooth increase of ion upflow in the present study may well be caused by the flux increase of energetic particles associated with the ICME rather than the ICME itself. Unfortunately, ICMEs arrived when EISCAT was observing near midnight, and hence we cannot single out any of these candidates as the direct trigger of ion upflow on the dayside.

As mentioned in subsection 3.4, the Svalbard 42 m antenna detected many short-lived enhancements of upflow as fast as 100 m/s at 400 km altitude in the period approximately from 05 to 11 UT on 7 September (Figure 6c). The enhancement started during northward IMF periods, and the upflow velocity started to decrease after the southward turning of IMF. The observation is unexpected because statistics from the same radar showed a higher upflow flux for southward IMF than northward IMF by nearly a factor of two (Ogawa et al., 2009). However, reduction of the upflow immediately after a southward turning of IMF in a case study does not necessarily contradict the statistics by Ogawa et al. (2009), because statistics during southward IMF are biased by the occurrence of the magnetic storms that are more common after ICME arrivals with southward IMF. A magnetic storm is known to enhance the ion escape by orders of magnitude (Moore et al., 1999; Slapak et al., 2017, and references therein). If we subtract this effect to extract pure effect through the dayside route only, the southward IMF may decrease the outflow by transferring the majority of the solar wind energy directly to the nightside over the high-latitude polar cap rather than deflected into the cusp

and its vicinity. In fact, the cusp size shrinks during southward IMF compared to northward IMF (Newell et al., 1989). A separate study with detailed examination of the timing is needed to investigate this problem.

A similar IMF dependence exists during approximately 11–12 UT on 8 September, when the IMF changed from northward to strongly southward (Bz about −17 nT). The EISCAT Svalbard radar at near local noon detected the cusp signature until 11:20 UT with substantial upflow flux during northward IMF. This is consistent with the conditions for upflow related to ion heating, which is maximized in the cusp (e.g., Nilsson et al., 1996, 2008). After the southward turning of IMF, the cusp moved equatorward to outside the radar's target area, and hence the low altitude ion heating in the radar's target area was no longer sufficient to accelerate the ions upward against gravity. This caused a reduction of the ion upflow velocity of the heated ions that are transported by the strong convection to this latitude (Ogawa et al., 2009). A similar explanation may apply for the lower upflow velocity after 12:00 UT on 8 September (exiting from the cusp by the southward turning of IMF) than before 10:00 UT (on the prenoon side of the cusp) when the IMF was pointing northward. In both cases, the upflow velocity at a fixed geographic location decreased with the southward turning of the IMF, contrary to the statistics.

The IMF control of the horizontal convection (subsections 3.3 and 3.5) generally agrees with past studies: the convection is enhanced during southward IMF with the area of convection expanding (or convection reversal moving) equatorward. One notable observation in terms of the dynamics is the substorm-like motion of the auroral arc during a very weak IMF (3 nT) with nearly zero northward component, at around 23 UT on 6 September before the first ICME arrival. The breakup of the auroral signature at local midnight took place at around 70° CGLat without significant geomagnetic signature. Even the geomagnetic station under this auroral arc (BJN in Figure 1j) did not detect notable magnetic deviation. In this sense it is not an ordinary substorm. We have not identified the cause of such a substorm-like auroral activity. The SEP event is the only event we have found so far that preceded before this activity, but this could well be a pure coincidence.

5. Conclusion

During 6–8 September 2017, EISCAT observed intermittent but significant ion upflow ($10^{12–13}$·m^{-2}·s^{-1}) already at as low as 400 km altitude during the entire period, with the intensity slightly increased if we compare the prenoon region over consecutive days after the X flares and ICME arrivals. While the general features of the ion outflow are consistent with our past knowledge, the observations showed some new features and raised questions. (1) The observed increase of the upflow was not triggered by the observed X9.3 X-ray flare, although they most likely contributed the preconditions, such as ion heating, for increased upflow. (2) The present observations could not distinguish the driving factor of the observed increase of the ion outflow among the enhanced solar wind, the SEP events, or the geosynchronous proton events. Dedicated studies are needed to find out the relative importance of the ICME arrival, a SEP event, and a geosynchronous proton event on the ionospheric heating and ion upflow. (3) The observations also showed a possibility that southward IMF does not necessarily enhance the local upflow but may suppress it. While this is consistent with the major destination of the solar wind energy during southward IMF, this also needs further studies. (4) Finally, the Tromsø VHF radar detected substorm-like auroral arc motions, first moving equatorward and then expanded and breaking up at around 70° CGLat, but without outstanding geomagnetic signatures. This is a complete puzzle. We do not even know whether it is associated with the SEP event at all. We need to make further investigations, including finding more cases.

Acknowledgments
We thank the following teams/institutions/organizations for operating and providing data that are used in this paper. ACE data (Figure 1) are provided by the ACE/SWEPAM, ACE/MAG, and ACE/EPAM teams through the ACE Science Center website (http://www.srl.caltech.edu/ACE/ASC/level2/index.html). GOES SEM data (Figure 1) are provided by GOES/XRS and GOES/EPS teams through NOAA National Geophysical Data Center (NGDC) GOES website (https://www.ngdc.noaa.gov/stp/satellite/goes/index.html). Geomagnetic indices (Figure 1) are provided by Data Analysis Center for Geomagnetism and Space Magnetism, Kyoto University, with raw data provided by geomagnetic AE, SYM/ASY, and Dst stations, and the indices are obtained from http://wdc.kugi.kyoto-u.ac.jp/aeasy/index.html. The EISCAT 5-min averaged data used in this paper (Figures 2–4) are available in ASCII format as supporting information. The EISCAT common programme data (Figures 2–6) are available to scientists of the member organizations for the first year and will become publicly available afterward at https://www.eiscat.se/madrigal/. The Norwegian ground magnetometer data (Figures 1 and 6) are produced by TGO (a coauthor's affiliation) and are available at http://flux.phys.uit.no/geomag.html. EISCAT is an international association supported by research organizations in China (CRIRP), Finland (SA), Japan (NIPR), Norway (NFR), Sweden (VR), and the United Kingdom (NERC). The work is partly supported by Swedish National Space Agency. We thank I. Häggström for the advice on the technical properties of the EISCAT radars.

References

Aikio, A. T., & Selkälä, A. (2009). Statistical properties of Joule heating rate, electric field and conductances at high latitudes. *Annales de Geophysique*, *27*(7), 2661–2673. https://doi.org/10.5194/angeo-27-2661-2009

Akasofu, S.-I. (1981). Energy coupling between the solar wind and the magnetosphere. *Space Science Reviews*, *28*(2), 121–190. https://doi.org/10.1007/BF00218810

André, M., & Yau, A. (1997). Theories and observations of ion energization and outflow in the high latitude magnetosphere. *Space Science Reviews*, *80*(1–2), 27–48. https://doi.org/10.1023/A:1004921619885

Brekke, A., & Rino, C. L. (1978). High-resolution altitude profiles of the auroral zone energy dissipation due to ionospheric currents. *Journal of Geophysical Research*, *83*(A6), 2517–2524. https://doi.org/10.1029/JA083iA06p02517

Cully, C. M., Donovan, E. F., Yau, A. W., & Arkos, G. G. (2003). Akebono/suprathermal mass spectrometer observations of low-energy ion outflow: Dependence on magnetic activity and solar wind conditions. *Journal of Geophysical Research*, *108*(A2), 1093. https://doi.org/10.1029/2001JA009200

Davis, T. N., & Sugiura, M. (1966). Auroral electrojet activity index AE and its universal time variations. *Journal of Geophysical Research*, *71*(3), 785–801. https://doi.org/10.1029/JZ071i003p00785

Dmitriev, A. V., & Yeh, H.-C. (2008). Geomagnetic signatures of sudden ionospheric disturbances during extreme solar radiation events. *Journal of Atmospheric and Solar - Terrestrial Physics*, *70*(15), 1971–1984. https://doi.org/10.1016/j.jastp.2008.05.008

Enell, C.-F., Verronen, P. T., Beharrell, M. J., Vierinen, J. P., Kero, A., Seppälä, A., et al. (2008). Case study of the mesospheric and lower thermospheric effects of solar X-ray flares: Coupled ion-neutral modelling and comparison with EISCAT and riometer measurements. *Annales de Geophysique*, *26*(8), 2311–2321. https://doi.org/10.5194/angeo-26-2311-2008

Futaana, Y., Barabash, S., Yamauchi, M., McKenna-Lawlor, S., Lundin, R., Luhmann, J. G., et al. (2008). Mars Express and Venus Express multi-point observations of geoeffective solar flare events in December 2006. *Planetary and Space Science*, *56*(6), 873–880. https://doi.org/10.1016/j.pss.2007.10.014

Gonzalez, W. D., Joselyn, J. A., Kamide, Y., Kroehl, H. W., Rostoker, G., Tsurutani, B. T., & Vasyliunas, V. M. (1994). What is a geomagnetic storm? *Journal of Geophysical Research*, *99*(A4), 5771–5792. https://doi.org/10.1029/93JA02867

Iyemori, T. (1990). Storm-time magnetospheric currents inferred from mid-latitude geomagnetic field variations. *Journal of Geomagnetism and Geoelectricity*, *42*(11), 1249–1265. https://doi.org/10.5636/jgg.42.1249

Kirkwood, S., & Osepian, A. (1995). Quantitative studies of energetic particle precipitation using incoherent scatter radar. *Journal of Geomagnetism and Geoelectricity*, *47*(8), 783–799. https://doi.org/10.5636/jgg.47.783

Klumpar, D. M., Peterson, W. K., & Shelley, E. G. (1984). Direct evidence for two-stage (bimodal) acceleration of ionospheric ions. *Journal of Geophysical Research*, *89*(A12), 10,779–10,787. https://doi.org/10.1029/JA089iA12p10779

Lennartsson, O. W., Collin, H. L., & Peterson, W. K. (2004). Solar wind control of Earth's H^+ and O^+ outflow rates in the 15-eV to 33-keV energy range. *Journal of Geophysical Research*, *109*, A12212. https://doi.org/10.1029/2004JA010690

Moore, T. E., Lundin, R., Alcayde, D., Andre, M., Ganguli, S. B., Temerin, M., & Yau, A. (1999). Source processes in the high-latitute ionosphere, Chapter 2 in Magnetospheric Plasma Sources and Losses. *Space Science Reviews*, *88*(1/2), 7–84. https://doi.org/10.1023/A:1005299616446

Newell, P. T., Meng, C.-I., Sibeck, D. G., & Lepping, R. (1989). Some low-altitude cusp dependencies on the interplanetary magnetic field. *Journal of Geophysical Research*, *94*, 8921–8927. https://doi.org/10.1029/JA094iA07p08921

Newell, P. T., Sotirelis, T., Liou, K., Meng, C.-I., & Rich, F. J. (2007). A nearly universal solar wind-magnetosphere coupling function inferred from 10 magnetospheric state variables. *Journal of Geophysical Research*, *112*, A01206. https://doi.org/10.1029/2006JA012015

Newell, P. T., Sotirelis, T., Liou, K., & Rich, F. J. (2008). Pairs of solar wind-magnetosphere coupling functions: Combining a merging term with a viscous term works best. *Journal of Geophysical Research*, *113*, A04218. https://doi.org/10.1029/2007JA012825

Nilsson, H., Waara, M., Marghitu, O., Yamauchi, M., Lundin, R., Rème, H., et al. (2008). Transients in oxygen outflow above the polar cap as observed by the Cluster spacecraft. *Annales de Geophysique*, *26*(11), 3365–3373. https://doi.org/10.5194/angeo-26-3365-2008

Nilsson, H., Yamauchi, M., Eliasson, L., Norberg, O., & Clemmons, J. (1996). The ionospheric signature of the cusp as seen by incoherent scatter radar. *Journal of Geophysical Research*, *101*(A5), 10,947–10,963. https://doi.org/10.1029/95JA03341

Ogawa, Y., Buchert, S. C., Fujii, R., Nozawa, S., & van Eyken, A. P. (2009). Characteristics of ion upflow and downflow observed with the European Incoherent Scatter Svalbard radar. *Journal of Geophysical Research*, *114*, A05305. https://doi.org/10.1029/2008JA013817

Ogawa, Y., Fujii, R., Buchert, S. C., Nozawa, S., Watanabe, S., & van Eyken, A. P. (2000). Simultaneous EISCAT Svalbard and VHF radar observations of ion upflows at different aspect angles. *Geophysical Research Letters*, *27*, 81–84. https://doi.org/10.1029/1999GL010665

Peterson, W. K., Andersson, L., Callahan, B. C., Collin, H. L., Scudder, J. D., & Yau, A. W. (2008). Solar-minimum quiet time ion energization and outflow in dynamic boundary related coordinates. *Journal of Geophysical Research*, *113*, A07222. https://doi.org/10.1029/2008JA013059

Peterson, W. K., Collin, H. L., Lennartsson, O. W., & Yau, A. W. (2006). Quiet time solar illumination effects on the fluxes and characteristic energies of ionospheric outflow. *Journal of Geophysical Research*, *111*, A11S05. https://doi.org/10.1029/2005JA011596

Reames, D. V. (1999). Particle acceleration at the Sun and in the heliosphere. *Space Science Reviews*, *90*(3/4), 413–491. https://doi.org/10.1023/A:1005105831781

Redmon, R. J., Seaton, D. B., Steenburgh, R., He, J., & Rodriguez, J. V. (2018). September 2017's geoeffective space weather and impacts to Caribbean radio communications during hurricane response. *Space Weather*, *16*. https://doi.org/10.1029/2018SW001897

Schillings, A., Nilsson, H., Slapak, R., Wintoft, P., Yamauchi, M., Wik, M., et al. (2018). O+escape during the extreme space weather event of 4–10 September 2017. *Space Weather*, *16*. https://doi.org/10.1029/2018SW00188

Schillings, A., Nilsson, H., Slapak, R., Yamauchi, M., & Westerberg, L.-G. (2017). Relative outflow enhancements during major geomagnetic storms - Cluster observations. *Annales de Geophysique*, *35*(6), 1341–1352. https://doi.org/10.5194/angeo-35-1341-2017

Schunk, R., & Nagy, A. (2009). *Ionospheres: Physics, plasma physics, and chemistry*. Cambridge: Cambridge University Press.

Slapak, R., Nilsson, H., Westerberg, L.-G., & Larsson, R. (2015). O+ transport in the dayside magnetosheath and its dependence on the IMF direction. *Annales de Geophysique*, *33*, 301–307. https://doi.org/10.5194/angeo-33-301-2015

Slapak, R., Schillings, A., Nilsson, H., Yamauchi, M., Westerberg, L. G., & Dandouras, I. (2017). Atmospheric loss from the dayside open polar region and its dependence on geomagnetic activity: Implications for atmospheric escape on evolutionary time scales. *Annales de Geophysique*, *35*(3), 721–731. https://doi.org/10.5194/angeo-35-721-2017

Tjulin, A. (2017). EISCAT Experiments, technical document by EISCAT Scientific Association. Retrieved from https://www.eiscat.se/wp-content/uploads/2017/04/Experiments.pdf

Tsurutani, B. T., Judge, D. L., Guarnieri, F. L., Gangopadhyay, P., Jones, A. R., Nuttall, J., et al. (2005). The October 28, 2003, extreme EUV solar flare and resultant extreme ionospheric effects: Comparison to other Halloween events and the Bastille Day event. *Geophysical Research Letters*, *32*, L03S09. https://doi.org/10.1029/2004GL021475

Turunen, E. (1993). EISCAT incoherent scatter radar observations and model studies of day to twilight variations in the D region during the PCA event of August 1989. *Journal of Atmospheric and Terrestrial Physics*, *55*(4–5), 767–781. https://doi.org/10.1016/0021-9169(93)90019-U

Ulusen, D., Brain, D. A., Luhmann, J. G., & Mitchell, D. L. (2012). Investigation of Mars' ionospheric response to solar energetic particle events. *Journal of Geophysical Research*, *117*, A12306. https://doi.org/10.1029/2012JA017671

Wahlund, J.-E., Opgenoorth, H. J., Häggström, I., Winser, K. J., & Jones, G. O. L. (1992). EISCAT observations of topside ionospheric ion outflows during auroral activity: Revisited. *Journal of Geophysical Research*, *97*(A3), 3019–3037. https://doi.org/10.1029/91JA02438

Wannberg, G., Wolf, I., Vanhainen, L.-G., Koskenniemi, K., Röttger, J., Postila, M., et al. (1997). The EISCAT Svalbard radar: A case study in modern incoherent scatter radar system design. *Radio Science*, *32*, 2283–2307. https://doi.org/10.1029/97RS01803

Yamauchi, M., & Slapak, R. (2018a). Energy conversion through mass loading of escaping ionospheric ions for different Kp values. *Annales de Geophysique*, *36*(1), 1–12. https://doi.org/10.5194/angeo-36-1-2018

Yamauchi, M., & Slapak, R. (2018b). Cusp current system: An energy source view. In A. Keiling, O. Marghitu, & M. Wheatland (Eds.), *Electric currents in geospace and beyond, Geophysical Monograph Series* (Vol. 235, chap. 20, pp. 339–358). Washington, DC: American Geophysical Union and John Wiley. https://doi.org/10.1002/9781119324522.ch20

Yau, A. W., Peterson, W. K., & Shelley, E. G. (1988). Quantitative parametrization of energetic ionospheric ion outflow. In T. E. Moore, J. H. Waite, T. W. Moorehead, & W. B. Hanson (Eds.), *Modeling magnetospheric plasma beyond, Geophysical Monograph Series* (Vol. 44, pp. 211–217). Washington, DC: American Geophysical Union. https://doi.org/10.1029/GM044p0211